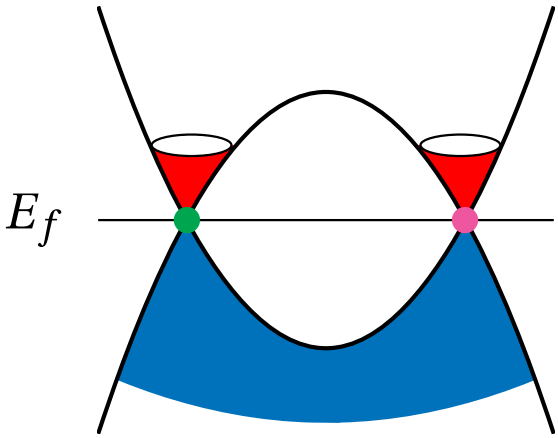

Transport Properties of Weyl Semimetal Mn_3Sn

Thesis

for the degree of

Master of Science

Author:

Ugnė Miniotaitė

Chalmers University of Technology

Gothenburg, Sweden. 2022.

Transport Properties of Weyl Semimetal Mn_3Sn

Ugnė Miniotaitė

June, 2022

SUPERVISOR
Priv.-Doz. Dr. Shibabrata Nandi
Jülich Centre for Neutron Science

EXAMINER
Ass. Professor Yasmine Sassa
Chalmers University of Technology

CHALMERS
UNIVERSITY OF TECHNOLOGY
Material Physics
Chalmers University of Technology

JÜLICH
Forschungszentrum
Jülich Centre for Neutron Science
Quantum Materials and Collective Phenomena

Gothenburg, Sweden. 2022.

Abstract

The antiferromagnetic Weyl semimetal Mn_3Sn has recently been of great interest because of exotic transport behaviors it exhibits at room temperature, such as Planar Hall Effect (PHE), large Anomalous Hall Effect (AHE) and negative magnetoresistance (MR). These exotic behaviors, rarely found in antiferromagnets, have potential to be utilized in future spintronics devices.

Mn_3Sn compounds need to be stabilized in excess of Mn, which means that the actual composition is $Mn_{3+\delta}Sn$ for $\delta \in [0.05, 0.3]$. Reports of the different exotic effects and other properties are therefore often attained from samples with varying Mn concentrations. In this thesis, we present extensive measurements of both magnetic and electronic transport properties of $Mn_{3.13}Sn$ for a wide temperature range, with the goal to map all the transport properties of Mn_3Sn for a single compound.

All measurements have been conducted at the Jülich Centre for Neutron Science (JCNS) using the Quantum Design Physical Property Measurement System (PPMS) and Magnetic Property Measurement System (MPMS). We are able to identify three transition temperatures of $Mn_{3.13}Sn$; $T_f = 45\,\mathrm{K}$, $T_t = 245\,\mathrm{K}$ and $T_N = 410\,\mathrm{K}$. Below T_f, we confirm a weakly ferromagnetic phase with magnetic easy direction [0001]. AC susceptibility measurements also reveal a slight glassiness in this phase, consistent with the previous reports. Furthermore, MR measurements display competing Weak Localization and Anti-weak Localization effects below T_f. T_N is identified as the Néel temperature above which the antiferromagnetic structure is destroyed.

Above T_t, we clearly observe PHE, AHE as well as negative MR. Between $T_f < T < T_t$ the Mn moments order in a spiral structure. In this temperature range both PHE, AHE and negative MR vanishes, consistent with earlier reports. We identify a six-fold anisotropy in magnetization confirming a triangular antiferromagnetic spin structure above T_t and observe the lowest-energy direction in the triangular configuration to be $[11\bar{2}0]$. This phase is also weakly ferromagnetic, and we find the easy direction to be in $[11\bar{2}0]$ direction for low external magnetic field which shifts to [0001] at a high magnetic field. To further characterize the change in lowest-energy direction we suggest a more detailed study.

Keywords: Weyl Semimetal, Topological Materials, Planar Hall effect, Anomalous Hall effect, Mn_3Sn, Weak Localization, Weak Anti-Localization, Chiral Anomaly

Acknowledgements

I want to first of all give a big thanks to Jülich Centre of Neutron Science for letting me conduct such an interesting project, and allowing me to use their great facilities. Furthermore, I want to thank my supervisor Shibabrata Nandi, for guiding me in the experimental work, and pushing to work independently. A really big thanks to Venus Rai, for all the hours of help in the lab, and the questions answered, and thanks to Subhapdip Jana, for preparing samples for me to use.

A really massive thank you to Albin, for helping me solve all my formatting problems, and for managing my anxiety.

Finally, ačiū tau tėtę, kad visada man padėjai savimi moksluose pasitikėti, ir, kad visada paklausei, kai man reikėjo su kažkuo garsiai pagalvoti.

Contents

1 Introduction

The electron band model, describing electron energy bands, has been a very successful tool used to categorize materials by conduction, separating materials into metals, semiconductors and insulators. An insulator is known to be non conducting, because of a finite energy gap, separating the conduction and valence bands. This essentially describes the historical use of the electron band model, as mainly a tool to categorize materials by their electron energy gap, or overlap of electron bands. This suddenly changed, with the experimental discovery of the topological insulator (TI), 15 years ago [1]. The TI acts as a normal insulator in the bulk, but at the surface it is conducting, through topologically protected surface states. The surface states' topological nature makes them robust against perturbations [2]. The discovery of the TI opened up a new area in condensed matter physics called topological materials, which are materials identified by having a non-trivial electronic band topology, leading to exotic transport effects. Recently, magnetic topological materials have been of great interest, and one such material is the Weyl semimetal (WSM) [3].

The WSM is a topological semimetal, where the conduction and valence bands meet at linearly dispersed points called Weyl nodes [4]. The nodes are topologically protected and can be seen as quasi-particles, acting as so called Weyl fermions. These quasi-particles, give rise to very exotic transport properties, such as for example Anomalous Hall Effect (AHE), in which a Hall voltage appears without the presence of a magnetic field.

Lately antiferromagnetic WSMs have been of great interest, because of their potential in spintronic applications. In spintronics, antiferromagnets have for long been of great interest, since they are robust against magnetic perturbation, produce no stray field and display ultrafast dynamics [5]. However, antiferromagnets struggle to produce a signal large enough for the devices. Antiferromagnetic WSMs exhibiting exotic transport phenomena offer the solution, and have therefore triggered extensive research in the area [6]. One of these antiferromagnetic WSMs is Mn_3Sn.

Mn_3Sn has been shown to have exotic transport phenomena, such as AHE, Planar Hall effect (PHE), and negative magnetoresistance (MR). The first step in being able

to tune and use these properties is to map them, and to understand their dependencies. To synthesize Mn_3Sn, it needs to be stabilized in excess of Mn, making the real composition $Mn_{3+\delta}Sn$ for $\delta \in [0.05, 0.3]$. The reports of different transport phenomena and their exotic effects, are therefore often attained from samples of varying Mn concentration, making it difficult to connect how all of these effect might appear for one compound. In this thesis we present a thorough investigation of the magnetic and electronic transport properties of the single crystal $Mn_{3.13}Sn$, with the aim to map its transport properties over a wide temperature and magnetic field range. We also aim to explore the sub 50 K region for which there are conflicting reports.

1.1 Thesis Outline

Section 2 begins by setting a foundation on topology of electron bands, to enable the reader to understand the mechanism giving rise to the WSM, and presents what is so far known about Mn_3Sn. Section 3 introduces the transport properties being measured in this thesis, and gives the proper background to help later interpret results. Section 4 explains the experimental techniques and tools used in the measurements, and Section 5 presents and discusses the results obtained from measurements. Finally Section 6 gives conclusions and outlook of the thesis. Table 1 shows a list of acronyms commonly used in the thesis, and can be used as a reference throughout the thesis.

Table 1: *A list of acronyms used throughout this thesis.*

Acronym	Meaning
AHE	Anomalous Hall Effect
PHE	Planar Hall Effect
HE	Hall Effect
WSM	Weyl Semimetal
LMR	Longitudonal Magnetoresistance
TMR	Transversal Magnetoresistance
NMR	Negative Magnetoresistance
MR	Magnetoresistance
WL	Weak Localization
MR	Weak Anti-Localization
PPMS	Physical Property Measurement System
VSM	Vibrating Sample Magnetometry
MPMS	Magnetic Property Measurement System
ACMS	AC Magnetic Susceptibility
SQUID	Superconducting Quantum Interference Device

2 Topology of electronic bands

We will in the following section give an introduction on topology, going into topology of electronic bands, which will be used in the explanation of Weyl semimetals and their topological nature. The reader is expected to have basic knowledge of solid state physics, calculus and quantum mechanics.

To begin, let us briefly go into the mathematical definition of topology. Topology is a study shapes, spaces and properties which are preserved under continuous deformations, such a stretching or twisting. In topology, two objects are seen as equivalent if it is possible to continuously deform one into the other. This concept is called homeomorphism, and objects that are homeomorphic with each other share so called topological invariants [7]. To explain the concept of homemorphism and topological invariants, let us take the old joke that goes "A topologist is a person who cannot see the difference between a coffee mug and a doughnut". The explanation of this joke is that a coffee mug and a doughnut are homeomorphic and to a topologist, therefore equivalent. Figure 1 shows us how a coffee mug can be continuously deformed into a doughnut. In this case, the hole of the doughnut and hole of the mug handle are the topological invariant. If we tried deforming it into a sphere we would somehow have to rip apart the hole, making our deformation no longer continuous. Topological invariants can be many different things, such as an algebraic structure (e.g. a group), a number of connected points or even an integer number, as with the Chern number which will soon be explained [7]. The main point is that a topological invariant does not change under continuous deformation.

Let us now continue to the topology of electronic bands. Historically, we have categorized materials into metals, semiconductors and insulators based on their conductivity. An effective tool for this has been the electron band model, which describes the electronic structure of the material in reciprocal space. For insulators and semiconductors there exists a band gap between the conducting and insulating electron bands where there are no possible states. In a semiconductor this band gap is smaller,

Figure 1: *Illustration a mug continuously deforming into a torus. Source: Topology joke by Henry Segerman [8].*

and by introducing some defect or imperfection the material can become conducting [9]. In a metal the conducting band is always somewhat occupied so the material is always conducting. A semimetal is somewhere in between a metal and se semiconductor, meaning that there is a small overlap in the electron bands. Figure 2 shows a schematic of the electron band structure for metals, semimetals, and insulators.

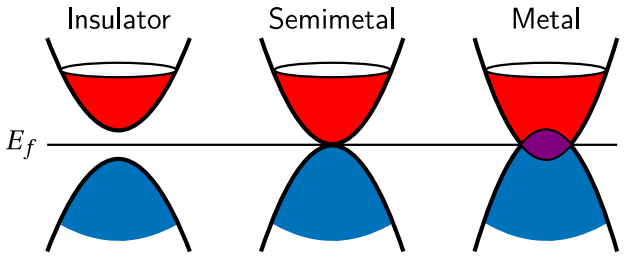

Figure 2: *Schematics of conduction (red) and valence (blue) bands for insulators, semimetals and metals. E_f denotes the Fermi level.*

In thermodynamics, we learn about phase transitions being connected to some kind of breaking of symmetry. However, in the past years, so called topological phases defined by the topology of the electronic bands, have been found. These topological phases are determined by something called Berry phase and its topological invariant is called the Chern number, which will be explained in the next section. For a more in depth mathematical view of topology of band structure the reader is referred to [10].

2.1 Berry phase and Chern number

Berry phase is a concept introduced in 1984 by Michael Berry [11] explaining adiabatic evolution of phase in quantum systems. In this section, we will describe the Berry phase quite conceptually. For a more mathematically in-depth description, the reader is referred to Berry's original work [11] as well as [12].

The Berry phase describes the picked up phase when a quantum mechanical state goes though a cyclic adiabatic evolution, i.e the phase obtained after traversing a closed loop in momentum space. The obtained Berry phase, $\gamma_n(C)$, for a state n over the closed path C, defining the boundary of the surface Σ, can be expressed in terms of the so called Berry curvature Ω_n as

$$\gamma_n = \iint_{\Sigma} d\mathbf{S} \cdot \Omega_m(R). \tag{1}$$

In electron bands, the Berry curvature is the quantity describing the entanglement between conduction and valence bands. Integrating the Berry curvature over a Brillouin zone gives you the Chern number, which is a topological invariant integer [13]. It is via the Chern number that electron band topological states are differentiated. Imagine a Hamiltonian describing the electrons in a lattice, which are separated into bands. The separated electron bands will still sense one another. The Hamiltonians will, because of this interaction, be adiabatically deformed, but with energy gaps kept open between the bands. Since the Berry curvature then varies continuously, the integral over the Brillouin zone, defined as the Chern number, cannot change since it is constrained to an integer. Now instead, if band gaps would close or open, the change is not adiabatic and there might be a change in the Chern number and therefore a phase shift.

2.2 Weyl Semimetals

In 1929, Hermann Weyl demonstrated, from Diracs equation, the existence of a massless fermions with finite chirality, which has later been named the Weyl fermion [14]. Chirality is a kind of asymmetry that we can think of as for hands; a left-handed chirality and a right-hand chirality. The total chiral charge is a conserved quantity [15]. The existence of Weyl fermions require the breaking of either time reversal symmetry or inversion symmetry, which for long was not believed to be possible. Time reversal symmetry describes the symmetry of physical laws moving forward or backward in time and inversion symmetry is the symmetry under point reflections. For a long

time, Weyl fermions remained undiscovered until they were found in Weyl Semimetals (WSM). A WSM is a semimetal where the conduction and valence electron bands cross in linearly dispersed points called Weyl nodes, and the points on or near the Fermi surface behave as Weyl fermions [4]. Figure 3 shows a schematic of such an electronic band structure.

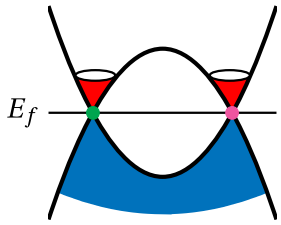

Figure 3: *Illustration of electronic band touching at Weyl nodes in a Weyl semimetal. Note the nodes different colors representing difference in chirality.*

The Berry curvature becomes singular at the Weyl nodes as either a source or a sink based on the chirality of the node. Chirality being a conserved quantity, together with the symmetry breaking, forces the Weyl nodes to arise in pairs of opposite chirality. These pairs give rise to a phenomenon called chiral anomaly. In a semi-classical regime the chiral anomaly can be understood as a pumping of charge carriers between two Weyl nodes of opposite chirality, when there is a parallel magnetic field and current within the plane of the Weyl nodes [16]. It is the chiral anomaly, which gives rise to interesting transport properties in Weyl semiemtals, such as negative magnetoresistance, PHE and AHE. One could intuitively think that a slight shift in energy would destroy the Weyl nodes, but because of the topological invariance of the Chern number, the Weyl nodes actually just move with the energy level in reciprocal k-space. This is the reason the exotic effects arising from the Weyl fermions are so robust.

The chiral anomaly also gives rise to surface states called Fermi Arcs, which create energy lines on the surface [17]. The Fermi Arcs can be measured using Angular Resolved Photoelectron Spectroscopy and are therefore a good way to study WSMs. The interested reader is referred to [17] to learn more about the historical background of the WSM, to [4] for a more in-depth conceptual view of chiral anomaly and to [18] for a mathematical approach to WSMs.

2.3 Mn_3Sn

Mn_3Sn is a hexagonal antiferromagnetic semimetal that has brought great interest because of its exotic transport properties at room temperature. There have been reports of AHE [19, 20], PHE [21] and negative MR [22], in Mn_3Sn at room temperature. In the following section, we will describe the crystal structure of Mn_3Sn, as well as what is so far known about its magnetic structure.

2.3.1 Crystal Structure

Mn_3Sn has a hexagonal crystal structure, which can be seen in Figure 4, and belongs to the space group $P6_3/mmc$. The Mn atoms are identified with different colors to illustrate the different crystal planes. Each Mn^{4+} ion has a large spin moment of about $2-3\ \mu_B$, and the Mn atoms form a layered kagome lattice along the z-direction [23–25]. A kagome lattice consists of equilateral triangles and hexagons, arranged in such a pattern that each hexagon is surrounded by triangles, and each triangle by hexagons. In recent years, kagome lattice metals have been studied extensively because of their topological electronic band structure often giving rise to exotic effects [26]. It has also been of interest, since system with kagome lattice structure display frustrations, which give rise to surprising/exotic magnetic phenomena.

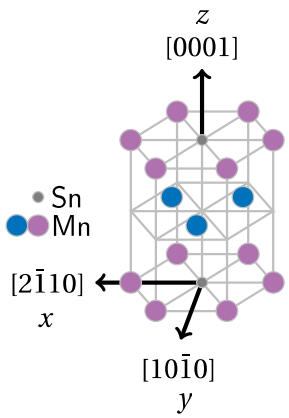

Figure 4: *Schematic of the hexagonal crystal structure of Mn_3Sn with crystallographic axes defined. Mn atoms are in different colors to differentiate between planes.*

Mn_3Sn can only be stabilized in excess of Mn, leading to Mn atoms replacing some of the Sn atoms [25]. With a lower Mn concentration, the sample becomes contaminated with Mn_2Sn. This translates to the actual composition of the crystal created

being $Mn_{3+\delta}Sn$ for $\delta \in [0.05, 0.3]$. The Mn concentration has been shown to affect the transition temperatures, and might be a vital knowledge to be able to tune the exotic transport effect [21].

2.3.2 Magnetic Structure

Three different magnetic structure regions of Mn_3Sn have been found, the exact temperatures of which vary, depending on report. There are some conflicting reports on what magnetic structure Mn_3Sn has at low temperatures, below transition temperature $T_f \sim 50\,\text{K}$. There are reports of there being a spin glass phase [27, 28], as well as a weak ferromagnetic order in the z-direction [24, 29]. Spin glass is a magnetic phase, where the magnetic spins are frozen in a disordered state, below a certain temperature. To further understand the mechanics of spin glass the reader is referred to the book "Spin Glasses" by Fischer and Hertz [30]. There is also a claim that the low temperature behavior is due to skyrmions [31]. A skyrmion is a magnetic state, which acts like a whirl of spins and are also a topological phenomenon [32].

Above T_f and below T_t, an antiferromagnetic spiral helix phase has been found, and above T_t, a co-planar triangular spin structure in the $xy-$plane has been identified [23, 29]. It is above T_t that the exotic chiral anomaly induced phenomena, in the xy-plane, are predicted [33]. This triangular spin structure is found up until the Néel temperature ,T_N, where the antiferromagnetic order is broken. Figure 5 shows a schematic of the different spin structures. Note that the different colored atoms represent different layers.

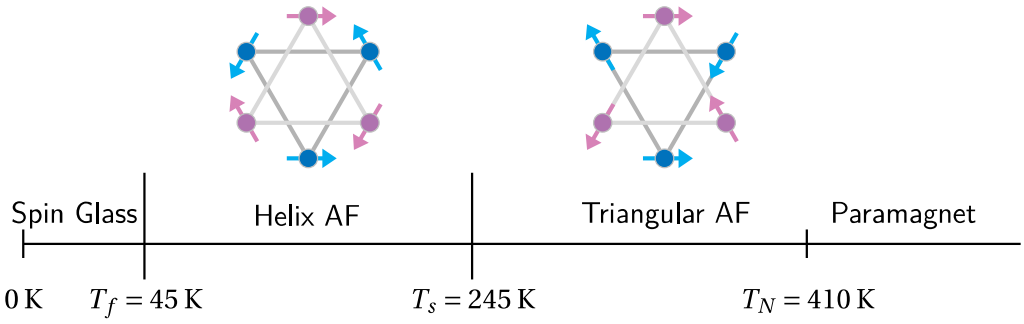

Figure 5: *Magnetic phases of Mn_3Sn illustrated according to temperature with an example spin structure for the Mn showed. The different colored Mn atoms are layered on top of each other.*

3 Transport Properties

In this section, we introduce the different transport properties that have been measured for this thesis. We explain the underlying effects causing the properties, and how they manifest themselves in the results as well as some artifacts coming from the sample shape. The reader is expected to have some basic knowledge of electromagnetism, solid state physics and quantum mechanics.

3.1 Magnetoresistance

Magnetoresistance (MR) is the property of a material to change its conductivity with applied magnetic field. If the magnetic field is applied in the direction of the electric field, the Drude model predicts that a drift velocity perpendicular to the magnetic field will be induced [34, chapter 3]. The electrons will drift away from path of conduction and the resistivity will therefore be higher. This is called the longitudinal MR. If the field instead is transversal to the current, a Hall voltage perpendicular to both will be induced, once again deflecting the charge carriers and increasing the resistivity with increased magnetic field. This is called transversal MR.

Using the two band model, one finds that as long as the number of charge carriers is finite, the MR will increase quadratically as B^2 [34, chapter 13]. This does not hold in a WSM, since the chiral anomaly, which can be seen as inducing charge carriers, gives rise to a higher mobility when magnetic field and current are parallel, leading to a negative MR (NMR). The NMR is an exotic effect and also a marker for chiral anomaly.

3.1.1 Weak Localization/Anti-Localization

A change from the classical MR does not only have to be due to chiral anomaly, but can also be caused by effects such as weak localization (WL) and weak anti-localization (WAL). These effects appear when the material is in the so called quantum diffusion regime. This phenomena appears at low temperatures when the phase coherence length is much longer than the mean free path, meaning that electrons will keep their phase even after being scattered many times [35]. In the quantum diffusion regime, the quantum interference between time reversed electron loops will give rise to a correction to the MR. WL refers to quantum interference between self crossing paths interfering negatively and therefore canceling, causing the resistance to become higher. WAL is when the trajectories interfere constructively and therefore amplify the conductivity. WAL gets destroyed by external magnetic field before WL making WAL more dominant at low fields. Lowering the temperature, moving further into the quantum regime, will make WAL becomes more prominent. This is a very simple way to describe the phenomenon and there is much more going into exactly why this happens. Interested readers are referred to [36].

3.2 Hall Effect

The Hall effect is an induced voltage, transvsersal to an applied current, arising due to an external magnetic field perpendicular to both the voltage and current [37]. Figure 6 shows how the electron path is curved and the transveral voltage induced. There are many analogous effects to the Hall effect. In this section we will present the Anomalous Hall effect (AHE) and Planar Hall effect (PHE).

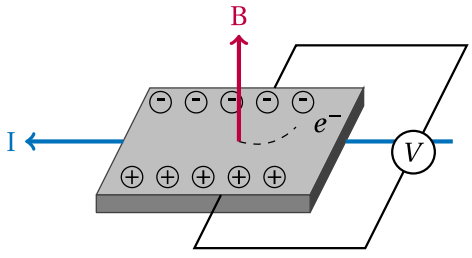

Figure 6: *Schematic of Hall effect. Lorentz force acts on the charge carriers (electrons, and holes), and creates a transversal voltage V.*

3.2.1 Anomalous Hall Effect

Anomalous Hall Effect (AHE) is a transversal Hall voltage, which appears in the same configuration as for the Hall effect, but without any external magnetic field applied. This phenomenon has long been observed in ferromagnets where the induced AHE voltage is proportional to the net magnetization [38]. However, for other materials, as well as some ferromagnets, there was for a long time no theory consistently predicting the AHE [39]. It was later found that the AHE was connected to both the material magnetization, and the Berry curvature [39]. In the example of a WSM, the topological Weyl nodes act as magnetic monopoles, mimicking the missing magnetic field, and in turn inducing the AHE. Therefore, even an antiferromagnet can exhibit AHE.

3.2.2 Planar Hall Effect

Planar Hall Effect (PHE) refers to a Hall effect where the induced electrical field, current and magnetic field all lie within the same plane [40]. The PHE has become a signature of the chiral anomaly. The chiral anomaly can be seen as a pumping of charge carriers when the magnetic field and current are in the same direction. The increase in charge carriers will also have an increase in drift velocity inducing a transversal voltage. This is the exact same mechanism inducing the NMR, and it is therefore not a surprise that the transversal electrical voltage is therefore proportional to the NMR with following angular dependency [41]:

$$\rho^{\mathrm{PHE}} = -\Delta\rho_{\mathrm{chiral}} \sin\theta\cos\theta = -\frac{1}{2}\Delta\rho_{\mathrm{chiral}} \sin 2\theta \tag{2}$$

$$\Delta\rho_{\mathrm{chiral}} = \rho_{\perp} - \rho_{\parallel}, \tag{3}$$

where ρ_{PHE} is the Hall resistivity, θ is the angle between the current and magnetic field, and $\rho_{\perp}$ and $\rho_{\parallel}$ are the transversal and longitudinal MR. Therefore, the PHE has its extremas at 45° and 135° whilst the regular Hall effect has extremas at 90° and 270°, making it easy to distinguish the two effects.

3.3 Magnetic Anisotropy

Magnetic anisotropy describes magnetic materials' properties being dependent on a direction of applied magnetic field. The direction that is the most easily magnetized is referred to as the materials' easy axis. Without magnetic anisotropy ferro- or ferrimagnetism would not be possible since these rely on the material spontaneously magnetizing in a certain direction. Magnetic anisotropy can be caused by different mechanisms such as shape, mechanical strain and crystal structure. In this section we will expand on shape anisotropy and crystal anisotropy by summarizing [42]. We refer readers seeking a deeper understanding of this book.

3.3.1 Shape Anisotropy

Shape anisotropy is the anisotropy arising due to shape asymmetry. Let us consider a polycrystalline sample which has no favorable orientation of the grains. In an applied magnetic field the sample should therefore be magnetized equally along all directions. However, if the sample is non-spherical, it turns out that it will magnetize easier along the longer axis than the shorter. This effect arises from the demagnetizing field being smaller in the longer direction than in the shorter. The demagnetizing field is the field arising from magnetic poles at the surface of a magnetized object acting in opposite of the field which produces it. A larger surface will therefore induce a larger demagnetizing field. It is this effect which gives rise to a magnetic anisotropy due to the shape. For a cuboid with different side lengths, it results in an anisotropy with 180° oscillations in magnetization, which can be describe by a $\sin 2\theta$ term.

3.3.2 Crystal Anisotropy

Crystal anisotropy is the magnetic anisotropy arising from the crystal structure of the material. This effect is mainly due to spin-orbit coupling, which refers to the coupling between the electron spin with the orbital motion of the electron. If an external field tries to reorient the electron spin, the orbit will also be reoriented. However, the electron orbit is strongly coupled to the lattice and will therefore resist this reorientation. It is this effect that is the cause of crystal anisotropy.

Since we are investigating the hexagonal lattice structure of Mn_3Sn, let us look at the crystal anisotropy of a hexagonal crystal. A schematic of a hexagonal system can be seen in Figure 7. The anisotropy energy depends only on the angle θ between the z ([0001]) axis and magnetization vector M_s, since the crystal is symmetric in the xy-plane. As written in [42], the anisotropic energy for a hexagonal system is defined as

$$E = \alpha_0 + \alpha_1 \sin^2\theta + \alpha_2 \sin^4\theta + \cdots \tag{4}$$

Depending on the sign of the coefficients, the easy axis where the anisotropy energy is at a minimum will be different. If α_1 and α_2 are positive, the easy axis will be along the z-axis. If the coefficients are negative, the easy direction will be in the xy-plane. From the anisotropy energy, we can calculate the torque excerpted on the system, which in turn tells us the magnetization behavior. The torque, L, is defined as

$$L = -\frac{dE}{d\theta} = -(\alpha_1 + \alpha_2)\sin(2\theta) + \frac{\alpha_2}{2}\sin(4\theta) = \alpha_1' \sin(2\theta) + \alpha_2' \sin(4\theta)$$

Since torque is connected to magnetic moment by $\vec{L} = \vec{m} \times \vec{B}$, and the angle between the magnetic field B and magnetization m is constant, the magnetization $\vec{m}$ will exhibit the same oscillatory behavior [43]. Therefore, magnetization will have a 2-fold and 4-fold symmetry for a hexagonal crystal. Even though it is clear what effects cause the crystal anisotropy, calculation of easy magnetization direction is still very difficult [42].

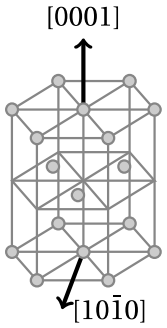

Figure 7: *Hexagonal lattice structure*

3.4 AC Magnetic Susceptibility

AC Magnetic Susceptibility (ACMS) is a sensitive tool for studying magnetic phase transitions and characterizing magnetic materials. In DC measurements, the sample is magnetized by a constant field and the equilibrium magnetization is measured. Such measurements produce DC magnetization curves $M(B)$, i.e. magnetization (M) versus magnetic field B. In AC measurements, a small AC field is superimposed on the DC field, causing a time dependence in the moment of the sample. This allows for measurements of dynamics not visible in DC measurements. When the AC frequency is low the magnetization measured can be expressed as:

$$M_{\mathrm{AC}} = \frac{dM}{dB} B_{\mathrm{AC}} \sin(\omega t),$$

where dM/dB is the slope of the DC $M(B)$ curve, which is also known as the susceptibility χ, H_{AC} is the AC magnetic field and ω is the frequency [44]. As the frequency increases, the sample will no longer follow the DC magnetization curve due to dynamic effects which cause the magnetization to lag behind the drive field. The AC susceptibility then yields two components, the amplitude of susceptibility χ and phase shift ϕ. Another representation is the susceptibility having a real in-phase component χ' and an imaginary out of phase component χ''. The two representations relate via.

$$\chi' = \chi \cos\phi, \tag{5}$$

$$\chi'' = \chi \sin\phi. \tag{6}$$

Both χ' and χ'' are sensitive to thermodynamic changes, and measuring ACMS is therefore a good tool to measure phase transitions. ACMS can be used for many things, such as characterizing superparamagnetism, superconductivity, and most relevant for this thesis is characterizing spin glass behavior [44].

Spin glass is a metastable state where the spins are disordered and frozen below a certain temperature. This freezing temperature can be determined by measuring χ' as a function of temperature, and identifying a cusp [44]. The irreversibility of spin glass also leads to a non zero χ'' below the freezing temperature [44]. The transition temperature cannot be extracted from the specific heat measurements and the ACMS measurement is therefore important. Furthermore, the way to specifically identify a spin glass is that the cusp is dependent of frequency which is unique for the spin glass [44]. Therefore, ACMS becomes a great technique to identify spin glass phases.

4 Experimental Techniques

In this section, we describe the experimental techniques used for the magnetic transportation measurements, and the experimental tools used and sample preparation.

4.1 Vibrating Sample Magnetometry

Vibrating Sample Magnetometry (VSM) is the most commonly used magnetometric technique to characterize magnetic properties in materials. The benefit of the VSM is the wide range of magnetic materials that it can measure as well as its time efficiency. A commercial VSM will be able to sweep magnetic fields from 2 mT/s up to 1 T/s [45]. One can measure samples such as solids, powders, single crystals, thin films or liquids using VSM [45]. Using an electromagnetic VSM, one can apply magnetic field up to 3 T, while a superconducting VSM will be able to reach fields of up to 16 T.

An electromagnet based VSM is constructed by an electromagnet with pickup-coils in between. The sample is then vibrated in the magnetic field created by the electromagnet, inducing a current in the pickup-coils. The resulting voltage induced over the coil is then proportional to the magnetic moment of the sample.

4.2 SQUID Magnetometry

Superconducting Quantum Interference Devices (SQUIDs) are the most sensitive magnetic flux detectors currently available and are used as highly sensitive magnetometers. A SQUID can measure any property which can be converted into magnetic flux; such as magnetic field, current, voltage, displacement, and magnetic susceptibility [46]. The Quantum Design Magnetic Properties Measurement System (MPMS-XL) SQUID, which has been used in this thesis, can measure magnetic flux change of 10^{-8} emu [47]. In this section, the principles behind SQUID will be explained as well as how it is being used as a magnetometer and erroneous artifacts to be aware of. The reader is expected to have some knowledge of superconductors.

4.2.1 Theoretical Explanation

The SQUID utilizes superconductivity, the Josephson effect, and magnetic flux quantization to measure small changes in the magnetic flux and in turn quantities such as magnetization. Magnetic flux quantization refers to the fact that magnetic flux passing through a superconductor is quantized in integer numbers of the magnetization quanta $\Phi_0 \approx 2 \times 10^{-15}$ Wb [48]. The DC Josephson effect says that if two superconductors are linked with a thin insulator, a current can flow without resistance through the link, up to some critical current, I_c, after which a voltage gets applied across the link. The current can flow without resistance due to quantum tunneling. This kind of junction is called a Josephson junction [48].

There are different types of SQUID, direct current (DC) and radio frequency SQUID. In this thesis, the DC SQUID has been used and will therefore be explained in more detail. The DC SQUID consist of a superconducting ring split up by two Josephson junctions symmetrically according to Figure 8. A (super) current is sent into the device and gets split in half to either arm of the ring. When a small external magnetic field is applied through the ring, it creates a screening current ,I_s, which induces a magnetic field opposite to what is applied inside the coil. As soon as either branch exceeds the critical current of the Josephson junction, a voltage appears across the junction. Suppose the flux through the loop then increases to above half a magnetic flux quanta, $\Phi_0/2$. Since the flux within the loop must be an integer amount of magnetic flux quanta, the superconductor will energetically favor to make the flux an even quanta of Φ_0 instead of screening. The screening current will therefore start to flow in the opposite direction. Thus measuring the applied voltage of the Josephson junctions can give the magnetic flux inside the coil within one magnetic flux quanta [48].

To be used as a magnetometer, the SQUID is coupled through an insulator junction with a pickup coil. The sample is moved through the coil inducing a current that is measured by the SQUID [46]. It is important to isolate the SQUID so that it does not sense the magnetic field going through the pick up coil.

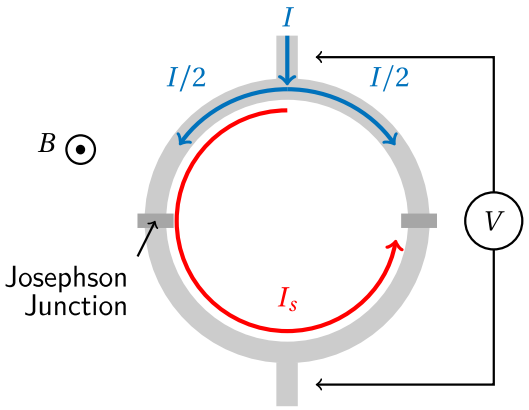

Figure 8: *Scheme of Superconducting Quantum Interference Device (SQUID) circuit.*

4.2.2 Errors in SQUID

Even though the SQUID theoretically has an accuracy of a single magnetic quanta ,Φ_0, there are errors arising from the setup that lower this resolution. The SQUID is ideal for measurements of a magnetic dipole, but in reality samples come in different shapes and sizes. Sawicki *et al.* conducted a study on the erroneous artifacts arising in the commercial MPMS SQUIDs [49]. They found errors in the measured magnetic moment arising from radial offset, axial offset, sample shape, sample holder and intrinsic effects in the pickup coil. As an example, they present a table of different cuboid shapes and the correction factors associated, which changes the collected data from ±1 % and ±4 % depending on the orientation of the sample. Sawicki *et al.* concluded that the theoretical resolution of 10×10^{-12} J/T could not be reached with a commercial MPMS SQUID and warn about interpreting data without considering these erroneous artifacts [49]. Matsumoto *et al.* [50] looked into radial offset effects in SQUID. They found that when a sample was mounted with a straw in a capsule and attempted to be centered, rotating the straw around its axis created a change of 3.2 % with an oscillatory behavior with a period of 360°. They also found that when the signal was minimal, the centering was the most accurate. Therefore, even a small off centering can cause a large change in signal and lead to oscillating behaviors when the sample is rotated.

4.3 Experimental Tools

This section describes the measurement tools used in the measurements included in this thesis.

4.3.1 PPMS

For measurements of Planar Hall Effect (PHE), Anomolous Hall Effect (AHE), AC Magnetic Susceptibility (ACMS), and DC magnetization, the in-house Quantum Design Physical Property Measurement System (PPMS) and DynaCool PPMS at the Jülich Centre of Neutron Science were used. These instruments can measure electrical transport, magnetization, AC susceptibility as well as thermal transport [51]. The PPMS uses VSM (see Section 4.1) to measure magnetization. Both the PPMS and DynaCool PPMS can produce a magnetic field in the range of −9 T to 9 T and go between temperatures of 1.9 K to 400 K. Although, using the VSM oven option one can go to temperatures up to 1000 K [51]. To be able to cool the system to the lowest temperatures, the PPMS uses liquid helium, whilst the PPMS DynaCool is completely cryogen free and uses two-stage Pulse Tube cooler instead [52].

The cooling mechanism is the main difference between the two systems. The PPMS also has a Rotator Option which was used to measure the PHE [53].

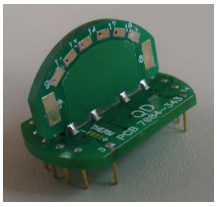

Figure 9: *In-plane rotation sample holder for the rotator Option of the PPMS.*

4.3.2 MPMS-XL

Conducting measurements of angular dependent magnetization of Mn_3Sn, the in house Quantum Design MPMS-XL SQUID Magnetometer at the Jülich Centre of Neutron Science with the Horizontal rotator Option was used. Figure 10 shows an illustration of the rotator sample holder, where the sample holder is rotated by the pulling of a wire. The rod is constructed to minimize the background created. The MPMS-XL uses a SQUID (read chapter 4.2) to measure magnetic moment or ACMS, to a maximum sensitivity of 10^{-11} J/T [51]. The MPMS-XL can be used in fields between −7 T and 7 T and temperatures between 1.9 K and 400 K.

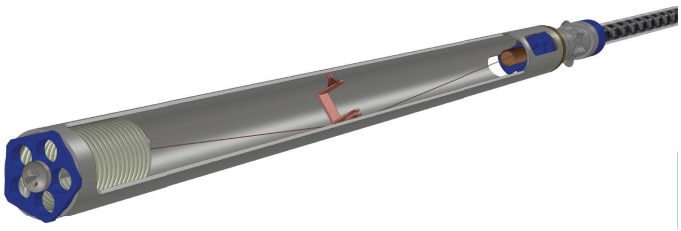

Figure 10: *Illustration of Quantum Design MPMS-XL Horizontal Rotator Option Sample holder (Image source [54]).*

4.3.3 Laue Camera

To identify crystallographic axes of the sample the in-house MWL120 Laue camera at the Jülich Centre of Neutron Science was used [55]. The camera is equipped with a multiwire detector and the X-rays produced from a tungsten tube. It has motorized goniometers, which allows for real time adjustments of the sample during measurement. Figure 11 shows an example of a diffraction pattern of one of the crystals. There are two superimposed hexagonal patterns indicating that the sample is multi grained.

4.4 Sample Preparation

To create the single crystal $Mn_{3.13}Sn$ sample Mn and Sn in the stoichiometric ratio 3.10:1 was melted using an induction melting technique in argon atmosphere to ensure the homogeneous mixing of the two elements. The alloy was then sealed in a quartz tube, in argon atmosphere, and heated to 1273 K for 12 hours, after which it

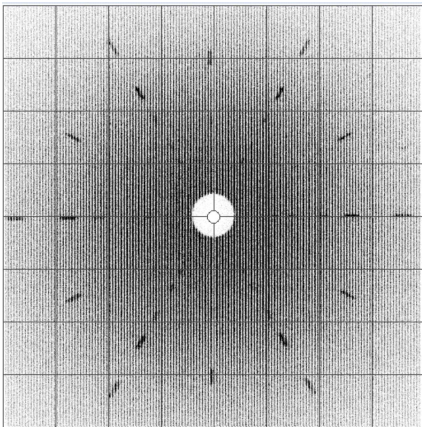

Figure 11: *Laue diffraction pattern of* Mn_3Sn *sample in the* [0001] *direction with a visible multi grain superposition of hexagonal patterns.*

was cooled at a rate of 2 K/min down to 973 K. Finally, the sample was quenched in water to cool it down to room temperature. The chemical analysis of the single crystal compound was conducted using the ICP-OES method. The chemical composition of the samples was found to be $Mn_{3.13\pm0.02}Sn$. Note that the author of this thesis did not create or chemically analyze the compound. The authors involvement was preparing the samples as described below.

To create the sample pieces, large single crystals were broken up using a hammer, where the newly exposed surfaces were inspected using the Laue-MWL camera. Figure 12 shows such a crystal to the left. After determining the crystallographic direction, the sample was cut using a diamond saw and then polished into suitable dimensions. Since the camera's motors are controlled by hand an angular offset of about $\pm5°$ of the crystallographic direction can be estimated. The samples were then measured by hand with an estimated accuracy of 0.05 mm. To mount the sample for magnetic measurements in the MPMS or PPMS Ge varnish was used. To conduct the electrical transport measurements, platinum wires were mounted onto the sample using epoxy paste. Silver paste was used to connect the wires to the sample platforms. Figure 12 shows a polished sample with attached platinum wires to the right.

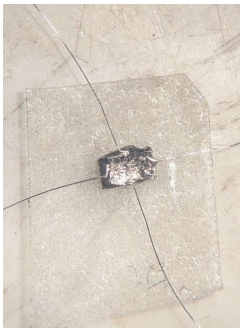

Figure 12: *Crystal piece of* Mn_3Sn *after being broken with a hammer to the left. Crystal after being polished and with attached Hall contacts with platinum wires on the right.*

5 Results and Discussion

The following section presents the results of different electronic and magnetic transport measurement on $Mn_{3.13}Sn$, which for brevity will be referred to as Mn_3Sn in the rest of the section. The crystallographic directions are often referred to as x, y, or z according to Figure 4. The results are divided up according to type of transport property, and to make it easy for the reader to digest, the results are discussed under the same section. Overarching conclusion based on these discussions are presented in the Section 6.

5.1 Magnetic Properties

The following measurements were conducted using the in house PPMS and PPMS Dynacool at Jülich Centre for Neutron Science, using the VSM option. Figure 13 shows the magnetization measurement $M(T)$ under heating of Mn_3Sn with magnetic field in x- and z-direction, for both Zero Field Cooling (ZFC) and Field Cooling (FC) in an applied field of 0.1 T. From this three transition temperatures can be identified: 45 K, 245 K and 410 K. The transition at 410 K corresponds to the Néel temperature T_N, below which Mn moments are antiferomagnetically ordered in a triangular magnetic structure. The Néel temperature has been previously found to be at around 420 K for Mn_3Sn [23]. We can identify T_t = 245 K, below which the Mn moments transform to an antiferromagnetic hellical spin structure [23, 29]. The triangular spin structure has also been found to be weakly ferromagnetic, but the easy axis has been debated. Kübler and Snadratski [24] calculated for the easy axis to be in the xy plane and Duan *et al.* [56] found a field dependence of the easy axis above T_t. Finally the transition at 45 K is a transition that has been found to go to a weakly ferromagnetic spin glass structure [27, 29]. Let us denote this transition temperature as T_f. Note the difference between ZFC and FC for temperatures above T_t and below T_f confirming that the material goes to a somewhat ferromagnetic state below T_f and above T_t. From Figure 13 it seems that at 0.1 T z-direction is favorable for low temperatures, and x-direction for high.

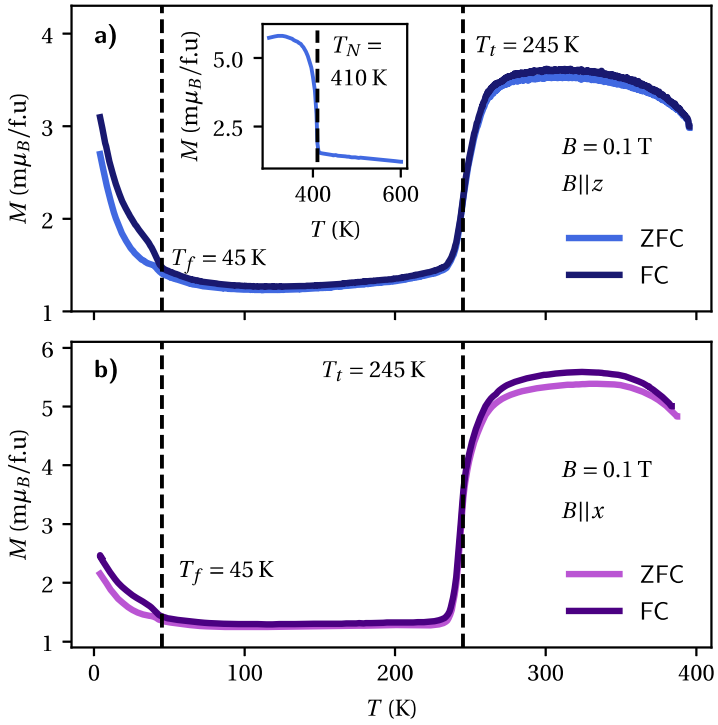

Figure 13: *Magnetization as a function of temperature for Zero Field Cooling (ZFC) and Field Cooling (FC) in* 0.1 T *with magnetic field parallel to z (a) and parallel to x direction (b). Inset in a) shows the ZFC for higher temperature.*

Figure 14 shows the magnetization curves $M(B)$ of Mn_3Sn with a comparison between x- and z-direction. From Figure 14, it is visible that there is a ferromagnetic moment at 4 K, as well as at 300 K, since the curves are not linear with the external magnetic field. The measurement of 300 K shows a magnetization hysteresis of around 0.15 T, and after that a linear behavior, whilst the 4 K data shows a larger S-shaped curvature, typical for ferromagnetic moment. It is therefore clear that the ferromagnetic behaviors are very different between the low and high temperature regions. It also seems that z-direction might be the magnetic easy axis at higher fields, but that x-direction might be favorable at lower fields. The measurements were taken on two different samples, therefore, one can not draw any clear conclusions of the field dependence of the easy axis from just Figure 14.

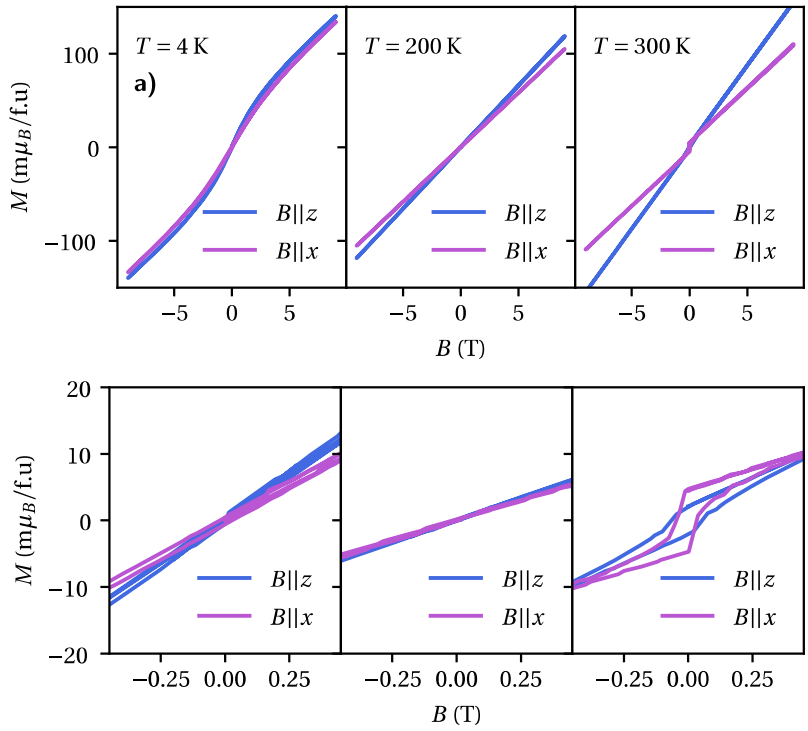

Figure 14: a) *Magnetization as function of external magnetic field for temperatures* 4 K, 200 K, 300 K *with field along x, and z.* ***b)*** *The same as* ***a)****, but zoomed in.*

Figure 15 shows the magnetization of the sample after the sample has been cooled in a field of 7 T from 300 K and then heated up again in zero field. We performed such measurements to see if there was any residual moment in the sample, which would indicate ferromagnetic moment present. From Figure 15, we can once again see the two ferromagnetic regions below T_f and above T_t. Let us once again highlight the difference in the ferromagnetic behavior. At zero field the triangular phase above T_t, shows a negative magnetization, whilst below T_f we see a positive magnetization. This difference might be due to the hysteresis above T_t and the residual field present (few μT) even if the field is set to zero. Figure 16 shows the magnetization curves,

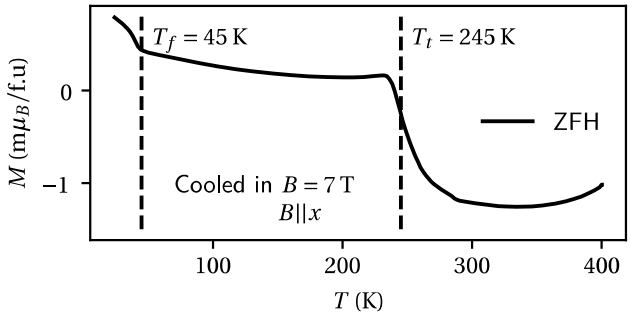

Figure 15: *Magnetization as function of temperature where sample has been cooled in* 7 T *and then heated up in zero field.*

$M(B)$, for temperatures around T_f and T_N. For low temperatures, it is clearly visible how the ferromagnetic curvature increases with lowered temperatures. For high temperatures, the transition is more abrupt, and wee see how the hysteresis disappears above 410 K. These results confirm the transition temperatures found in Figure 13.

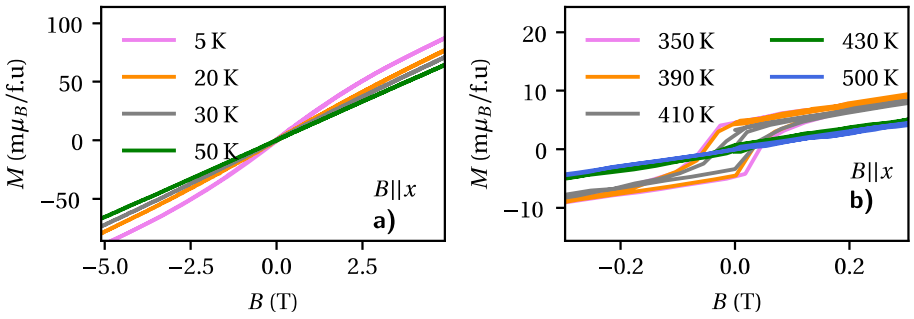

Figure 16: ***a)*** *Magnetization as a function of external magnetic field for transition below* $T_f = 45$ K. ***b)*** *same as in* ***a)****, but for transition above* $T_N = 410$ K.

5.2 Magnetic Anisotropy

All measurements were conducted using the in-house Quantum Design MPMS-XL SQUID at Jülich Centre of Neutron Science using the Horizontal rotator Option [54] (see Section 4.3.2). Figure 17a) shows the angular dependence of magnetization in the xy-plane of Mn_3Sn for different temperatures, where the angle, crystallographic direction and direction of the external magnetic field are defined according to Figure 17c). A clearly visible 1-fold symmetry (360° oscillation) is present for all temperatures. It appears most likely due to extrinsic effects since the magnitude and phase of the oscillation does not change with temperature. It should be noted that for these measurements, the sample was mounted off center on the sample holder, which most likely amplified errors due to radial offset (see Section 4.2.2 for an explanation of radial offset and Section 4.3.2 for information about the sample holder). The data in Figure 17a) has not been offset in amplitude and it is therefore interesting to note that the overall signal gets larger with lower temperature. Further, we see that the 1-fold oscillations have an amplitude of about 2% to 3% of the total amplitude. Matsumoto *et al.* [50] found 360° oscillations with an amplitude up to 5% when rotating a capsule sample holder, which had been attempted to be centered. Since our sample was well off center to begin with, these oscillations are most likely due to the radial offset.

When fitting the data, the best fit was found using a superposition of a 1-fold, 2-fold, and 6-fold symmetry, yielding the following fitting function for the magnetization M:

$$M_{xy} = K_0 + K_1 \sin(\theta + \alpha_1) + K_2 \sin(2\theta + \alpha_2) + K_6 \sin(6\theta + \alpha_3), \tag{7}$$

where α_1, α_2, and α_3 are phases that can help determine the easy direction of magnetization. Figure 17b) shows the temperature dependence of the fitting coefficients. The errors of the fitting coefficient are in the order of 10^{-5} mμ_B/f.u, which means that the function fits the data really well. From Figure 17b) it is clear that both the 2-fold and 6-fold symmetry has a sharp increase at the transition temperature T_t of 245 K, where Mn_3Sn goes to a triangular spin structure from a helix spin structure. As stated before, we see that the 360° oscillations do not change much with temperature, but are very large in magnitude. The sharp increase in the 2-fold oscillation is most likely due to distortion of the equilateral triangular spin configuration as also found by Duan *et al.* [56]. The low temperature 2-fold oscillations are much smaller and could be an artifact of the sample shape anisotropy since the sample was a cuboid with dimensions 3.1 mm × 1.6 mm × 0.6 mm (each length measured with accuracy ±0.05 mm), which is far from spherically uniform (see Section 3.3.1).

The most notable result is the 6-fold symmetry arising at temperatures above the transition temperature 245 K, which was also found by Duan *et al.* [56]. These oscillations can be explained by anisotropy in the xy-plane $(10\bar{1}0)$ in the triangular spin structure, and this therefore enforces the transition from a spiral helix phase to triangular spin phase at 245 K. In Figure 17a), also shows how the measured data for 260 K can be broken down into the superimposed sinus curves used for fitting. Because of the erroneous artifacts arising from sample misalignment as well as measurement of sample weight, the absolute values should not be considered, only the relative behavior.

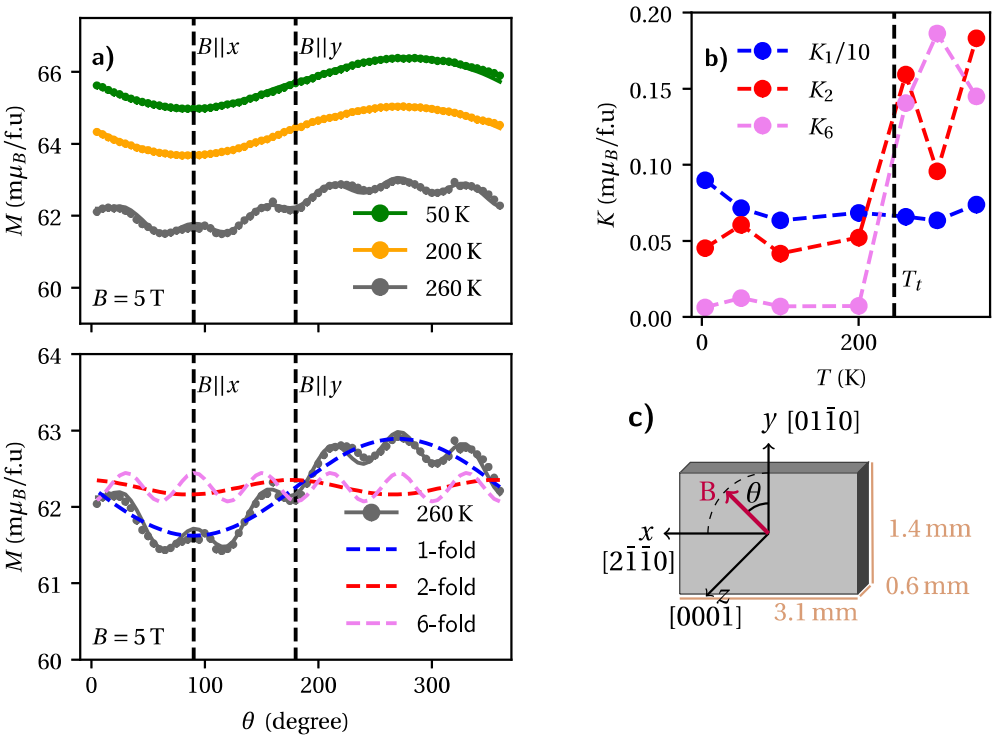

Figure 17: a) *Data points and fits of in-planar angular dependence of magnetization of* Mn_3Sn *at magnetic field of* 5 T *for* 50 K, 200 K *and* 260 K *(above), the* 260 K *data and fit with decomposition of fit.* ***b)*** *temperature dependence of fitting coefficients from equation 7.* ***c)*** *scheme of sample orientation, including dimensions of sample, magnetic field direction, and crystallographic direction.*

Figure 19 shows the angular dependent magnetization in xz-plane, with crystallographic axis, angle, and magnetic field direction defined according to Figure 18. Since there now is a rotation between crystallographically non-symmetric orientations, we

need to consider crystal anisotropy and therefore introduce a 4-fold term (see Section 3.3.2). We keep the 6-fold symmetry, even though it is expected to be absent, since the sample might be somewhat tilted, yielding a small 6-fold component. Therefore, our new fitting function takes the form:

$$M_{zx} = K_0 + K_1 \sin(\phi + \alpha_1) + K_2 \sin(2\phi + \alpha_2) + K_4 \sin(4\phi + \alpha_3) + K_6 \sin(6\phi + \alpha_4). \quad (8)$$

From Figure 19, we most notably see a clear 180° oscillation that varies in magnitude and phase depending on temperature. We see that there is a weak ferromagnetism for 260 K with the easy axis in z-direction. This is consistent with the results of Duan *et al.* [56]. In the spiral helix phase, there should not be any ferromagnetic moment, and we see that the amplitude of the oscillations is significantly smaller. As stated for the in plane rotation, the 180° oscillations might be due to the sample shape anisotropy, since our sample is significantly longer along the x-direction than z-direction (see Figure 18). The signal due to shape anisotropy is expected to be longer for external field parallel to x, which is exactly what we see. Coming down to 10 K, the ferromagnetic effects seem to reappear with the easy axis once again being in the z-direction, but the change in signal not being quite as strong. However, the overall signal is stronger.

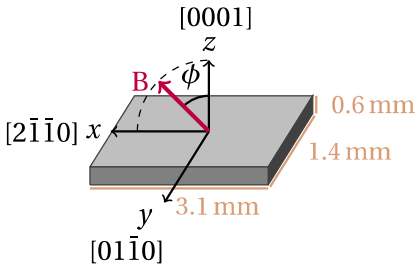

Figure 18: *Schematic of rotation angle, magnetic field direction, sample dimensions and crystallographic directions.*

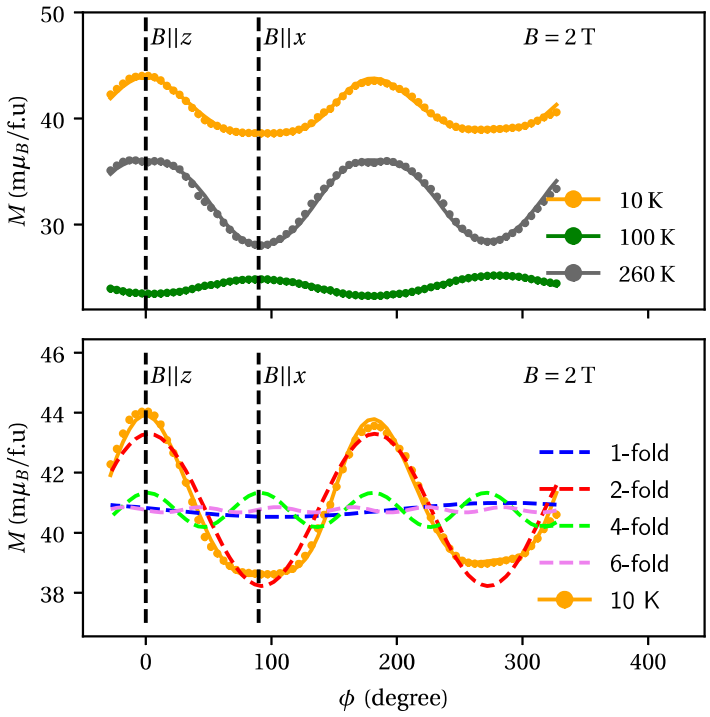

Figure 19: *(Above) Data points (dots) and fits (lines) of out measurement of angular dependent magnetization of* Mn_3Sn *at different temperatures. (Below) The* 10 K *data and fit, together with decomposition of fit. Angle of rotation defines according to Figure 18.*

In Figure 20, we see the data, fit and sinusoidal decomposition of angular dependence for 260 K for external magnetic field 2 T and 5 mT, respectively. It is clear how the effects of radial offset and shape anisotropy become more dominant at low field, while the ferromagnetic behavior takes over with higher field. We note that the fitting function fits well for the different field strengths, which indicates an accurate fitting function. We see that for low field, the 2-fold oscillation has the easy direction in x-direction instead, which is consistent with the results of magnetization in Figure 14, where magnetization along x-direction dominates at lower fields. We note that the magnitude of the low field oscillations are larger than the oscillations of the 100 K data if Figure 19 indicating that the change in easy axis is not merely a shape anisotropy effect. However, measuring the same effect on a more square sample shape would be needed to be able to map the field dependence of easy axis. The field dependence of the easy axis, which we have found is consistent with the results of Duan *et al.* [56].

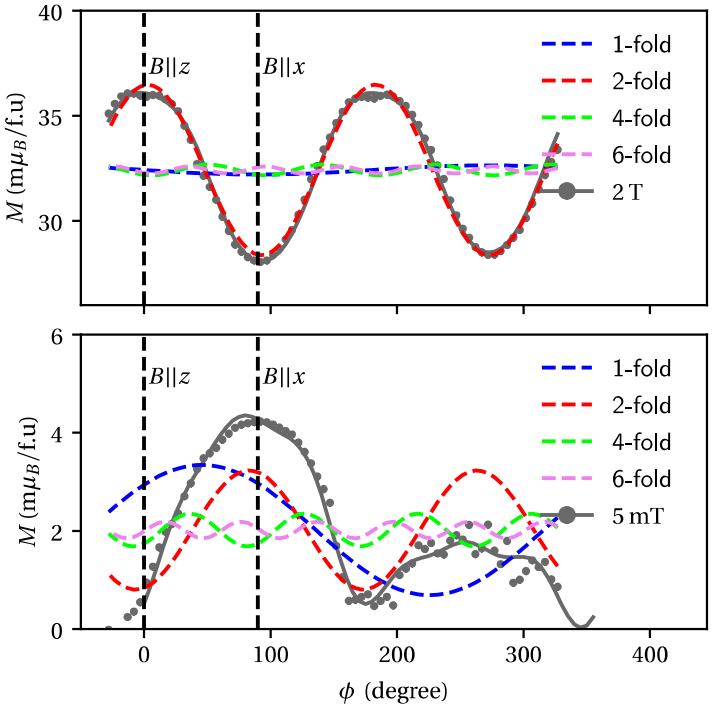

Figure 20: *Data points and fits of out of plane angular dependence of magnetization of* Mn_3Sn *at magnetic field for* 260 K *at* 2 T *(above) and* 5 mT *(below). Angle of rotation defines according to Figure 18.*

5.3 AC Susceptibility

Figure 21 shows the ACMS in-phase component $\chi'(T)$, while heating of the Mn_3Sn sample for different frequencies, with a 5 µT AC magnetic field in the z-direction. There is a visible change in cusp from around 26 K at 3 kHz to around 30 K at 10 kHz. The peak moving to higher temperatures with higher frequency, and the transition to a glassy phase being around 30 K is consistent with previous reports [27]. The sample mass was around 13 mg, which would explain the much smaller and less pronounced peak than in the other reports, where the sample mass was around an order of magnitude larger. It could also indicate that the glassy phase only applies to a quite small portion of the total spins.

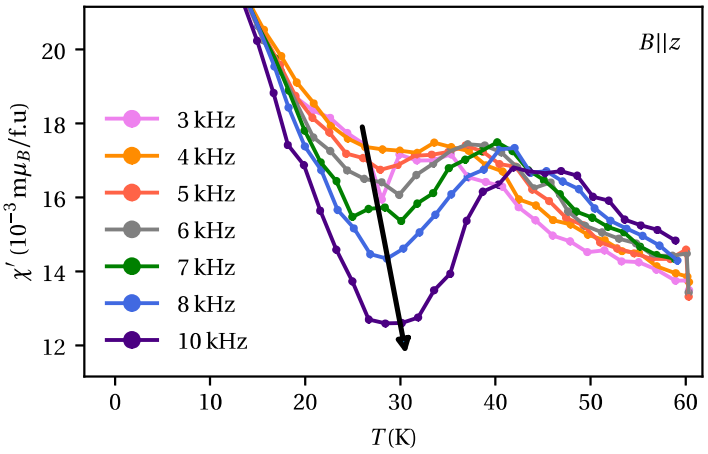

Figure 21: *Real part of AC Magnetic Susceptibility measurements for different frequencies, with magnetic field parallel to z-direction and AC magnetic field of* 5 µT.

Figure 22 shows the ACMS out-of-phase component $\chi''(T)$ for the same measurements as for Figure 21. We see the same type of shift in temperature with higher frequency. However, there seems to be a shift in the cusp temperature with almost 5 K. For a glassy phase, the imaginary, χ'', should increase below the freezing temperature, and stay increased. We see for lower temperatures the magnitude is higher than before the cusp.

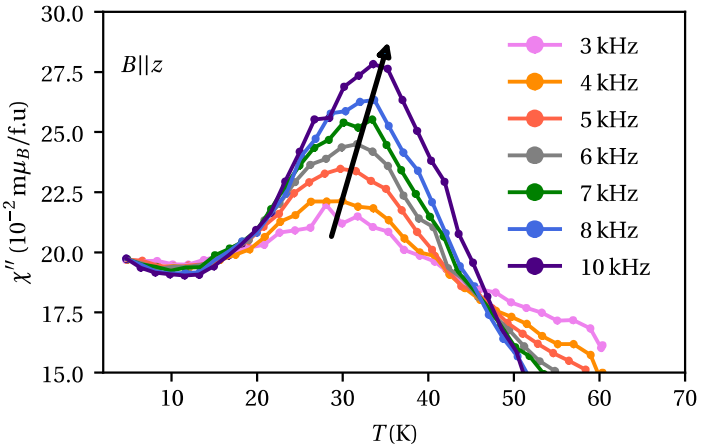

Figure 22: *Imaginary part of AC Magnetic Susceptibility measurements for different frequencies, with magnetic field parallel to z-direction and AC magnetic field of* 5 µT.

5.4 Magnetoresistance

In this section, we present measurements of longitudinal magnetoresistance (LMR) and transversal magnetoresistance (TMR). The sample dimensions, crysallographic directions and connection scheme in the measurements are according to Figure 23. In the following section all of the data of any MR measurement has been symmetrized and only the curves of going from a high absolute field to zero field have been used. This to avoid artifacts from hysteresis.

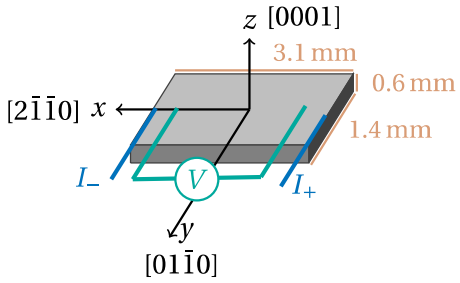

Figure 23: *Scheme for sample orientation for measurements of MR, including current direction, crystallographic direction, and voltage contacts.*

Figure 24a) shows the temperature dependent longitudinal resistance as a function of temperature at zero external field applied. We see a very smooth curve that follows the typical metallic behavior, where the resistivity ρ, increases with temperature [57]. Looking at the temperature gradient of the resistivity in Figure 24b), we find a kink at $T_t = 245\,\mathrm{K}$, which is what is expected at a phase transition. We note that no kink is seen at other temperatures, indicating that this is the only sharp transition within the measured temperature range.

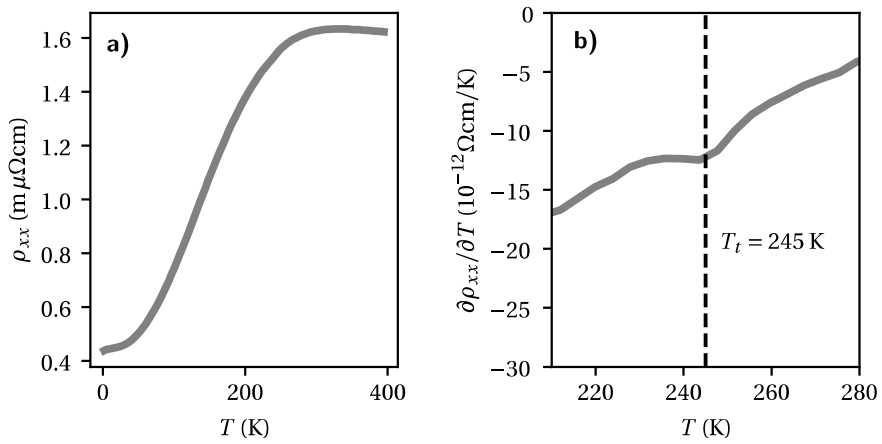

Figure 24: a) *Longitudinal resistance at zero field of* Mn_3Sn*, as a function of temperature.* ***b)*** *Temperature gradient of longitudinal resistance, with transition temperature* T_t*.*

Figure 25 shows the LMR of Mn_3Sn for temperatures going from 2 K - 50 K. Note that there is an offset between different temperatures, but that the scale of change is still accurate. We see that at 50 K the MR is quadratic as is expected in a semimetal. As the temperature decreases, a cusp near zero field appears, consistent with the effects of WL. As the temperature decreases, we see the cusp disappearing and a very high MR appearing. This is consistent with WAL, which becomes more dominant at lower temperatures. The steep increase at high field is most likely coming from the WL effect also getting stronger. This type of transition between WL and WAL has been found in other materials [58]. We see that the WL effects begin at around 30 K, which is the same temperature as the glassy phase transition. This indicates that 30 K is the temperature at which Mn_3Sn enters the quantum regime.

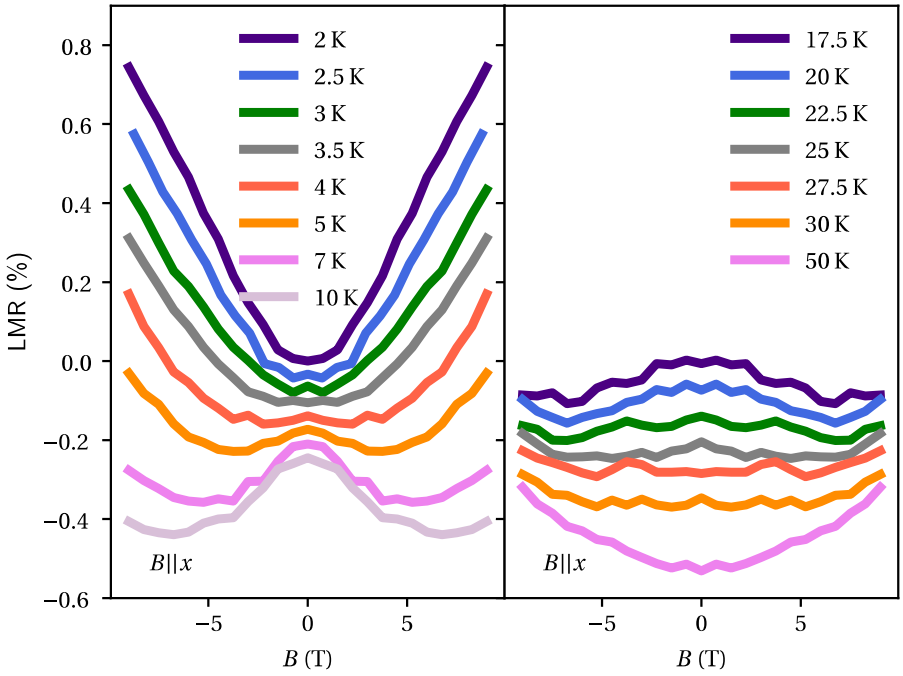

Figure 25: *Longitudinal MR with current and magnetic field along x-direction of* Mn_3Sn *for temperatures between* 2 K - 50 K.

Figure 26 shows the LMR and TMR near transition temperature $T_t = 245\ K$. We see that both the LMR and TMR exhibit a quadratic behavior up until transition temperature $T_t = 245\ K$. The LMR abruptly becomes negative, which is the signature of chiral anomaly due to Weyl nodes. This confirms the Weyl nature above T_t in the xy-plane, and is consistent with other reports [22]. It is also worth noting that that increase in MR becomes much sharper after transition in the TMR as well.

Figure 27 shows more measurements of LMR for Mn_3Sn past transition temperature $T_t = 245$ K. Please note that these measurements were conducted using the PPMS, whilst the previous (Figure 26) were using Dynacool PPMS, which has a higher resolution. It seems that the negative MR is the largest right above transition at 260 K and then slowly becomes less prominent.

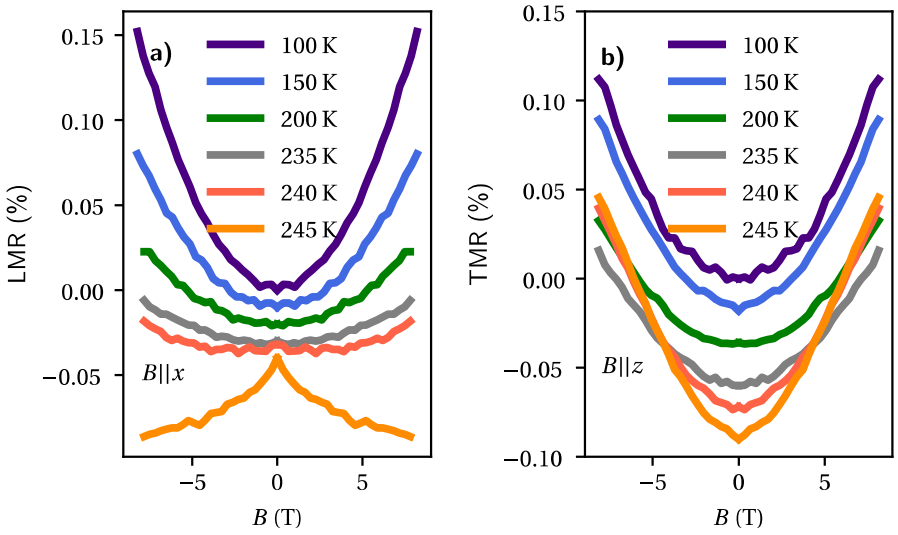

Figure 26: ***a)*** *Longitudinal MR of* Mn_3Sn *around transition temperature* T_t. ***b)*** *Transversal MR of* Mn_3Sn *around transition temperature* T_t.

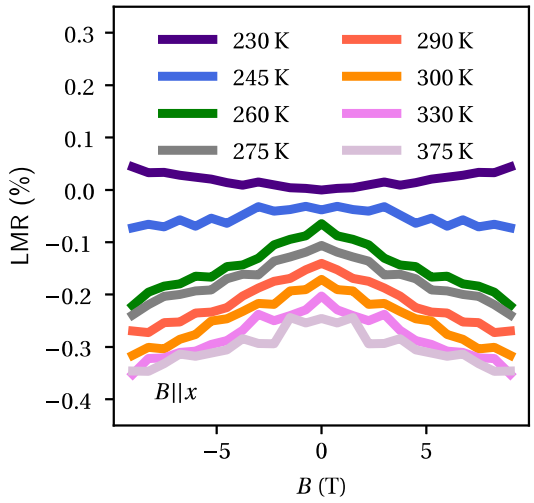

Figure 27: *Longitudinal MR of* Mn_3Sn *for multiple temperatures above* T_t*, with magnetic field in* x*-direction.*

5.5 Hall Effect

For the angular Hall Effect (HE) measurements, the rotational axis, current direction, magnetic field direction, and sample dimensions are according to Figure 28.

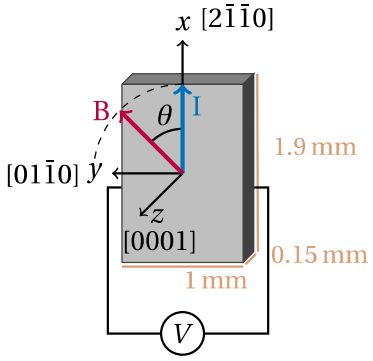

Figure 28: *Scheme for sample orientation for measurements of angular HE, including sample dimensions, crystallographic axes, current direction, and voltage connections.*

For the angular measurements, the Quantum design PPMS in-plane rotator sample holder (see Figure 9) was used. The sample holder has a slight tilt in the center mounting piece. Furthermore, the sample could be up to 5° misaligned in the z-axis, due to limitations of the sample cutting. Because of the tilt, the magnetic field and voltage directions have an additional component, not illustrated in Figure 28. To better understand how this affects the results, let us express the magnetic field, voltage, and current for $\theta = 90°$:

$$\vec{B} = B_z\hat{z} + B_y\hat{y}$$
$$V = V_y + V_z$$
$$\vec{I} = I_x\hat{x}.$$

The split contribution means that, apart from the PHE contribution to the signal, there might be a regular Hall contribution, from both the magnetic field in $y-$ and $z-$ direction. With rotation, the magnetic field component in z-direction will be constant and not oscillating. Therefore, any 360° oscillation in the angular resistivity would come from the magnetic field varying from y- to x-direction, and the voltage being measured along z. Since we were measuring the HE and PHE simultaneously, the collected data was fitted with a 360° oscillation, superimposed by a 180° oscilla-

tion, leading to the following fitting function:

$$\rho_{PHE} = K_{\mathrm{AHE}} \sin(\theta + \alpha_1) + K_{\mathrm{PHE}} \sin(2\theta + \alpha_2), \tag{9}$$

where K_{AHE} and K_{PHE} represent the amplitude of the HE and PHE, and α_1 and α_2 are their phases. Figure 30 shows the angular dependence of the PHE and HE for different temperatures, including their fits. It also shows the decomposition of the fit function for 260 K. It is visible, that the 180° oscillations diminish below $T_t = 245\,\mathrm{K}$, and that there is only a 360° oscillation left at 230 K.

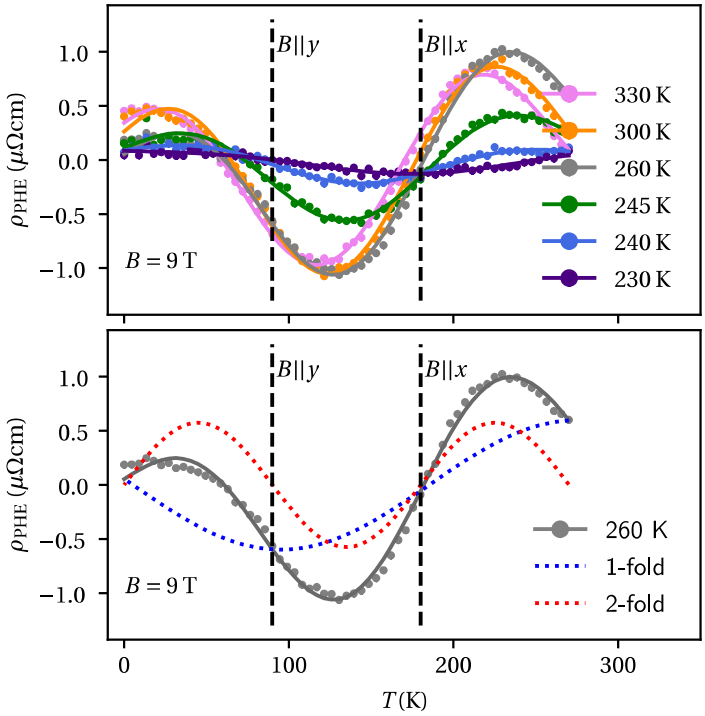

Figure 29: *(Above) Data points (dots) and fits (lines) of measurement of angular dependent HE and PHE of* Mn_3Sn *at different temperatures. (Below) the* 260 K *data and fit, together with decomposition of fit. Angle of rotation defined according to Figure 28.*

Figure 30a) shows the change in coefficients of fitting function 9, with regards to magnetic field, and temperature. Both the HE, and the PHE varying linearly with magnetic field is expected, since the force on charge carriers is linearly dependent of the magnetic field. However, it is interesting that the PHE and AHE have opposing slopes, indicating that they arise due to different charge carriers, which once again shows us

the difference in nature of these effects. Figure 30b) shows how the same coefficients vary with temperature. Here, the transition at $T_t = 245\,\mathrm{K}$ is really clear. We suspect that the jump in HE is due to the hysteresis from the AHE at zero field. Similarly as for LMR, above T_t, it seems that both the PHE and HE decrease as the temperature increases, which is expected.

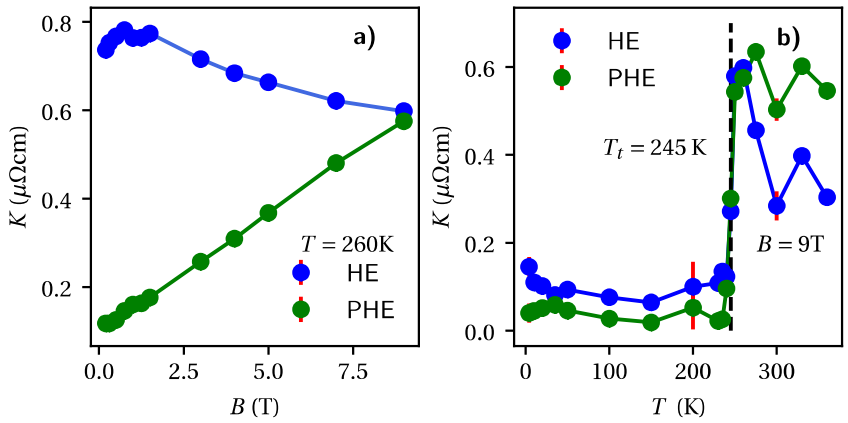

Figure 30: *Coefficients from fitting function in Equation (9), representing amplitudes of AHE and PHE varying with magnetic field (**a**) and temperature **(b)**, including error bars.*

The samples used were measured by hand, leading to an uncertainty of about $\pm 0.05\,\mathrm{mm}$, which is quite a large margin of error for a sample thickness of 0.15 mm. Therefore, it would not yield much, trying to fit the MR measurements to the PHE equation (2). Although, we can note that the PHE, LMR and TMR are of the same order of magnitude, $\sim 1\ \mu\Omega\mathrm{cm}$, which aligns with the theoretical prediction.

Using the same sample and configuration as in Figure 28, but with the field in z-direction, the magnetic field dependent Hall effect was measured. The measurement was conducted using the Dynacool PPMS system. Because of the same crystallographic tilt in the sample, a part of the magnetic field was in the xy-plane, meaning that the AHE contribution from the Weyl nodes in xy-plane was simultaneously measured. Figure 31 shows this measurement for 200 K and 260 K. We see a clear hysteresis appearing above the transition temperature T_t, clearly illustrating a Hall voltage at zero field. This confirms the presence of Weyl nodes in the magnetic triangular phase above $T_t = 245\,\mathrm{K}$. We can note that the HE has the same slope as in Figure 30.

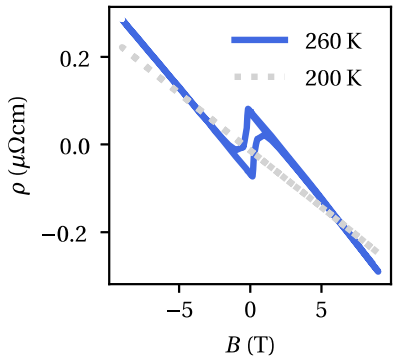

Figure 31: *Magnetic field dependent Hall voltage with magnetic field along $z-$axis, with a small component along y-axis, and current along x. Voltage is measured along y-axis with a small component along z.*

6 Conclusions and Outlook

In this thesis, we have presented a thorough investigation of the transport properties of the antiferromagnetic WSM $Mn_{3.13}Sn$, and have been able to identify three transition temperatures; $T_f = 45\,\mathrm{K}$, $T_t = 245\,\mathrm{K}$, $T_t = 410\,\mathrm{K}$.

Through ACMS measurements, a slight glassy phase below T_f (at $T \approx 30\,\mathrm{K}$) has been identified, consistent with previous reports [27, 28]. Starting from the same temperature of around 30 K, we observed competing WL and WAL effects, indicating a connection between the spin glass phase and the quantum regime of $Mn_{3.13}Sn$. Through both magnetization curves and magnetic anisotropy measurements, a weak ferromagnetic moment with easy magnetization in the z-direction below T_f has been found, consistent with previous reports [29]. However, the true origin of the ferromagnetism below T_f is far from clear. Since it seems to arise before the spin glass phase, one can assume that these two are not connected. A more thorough study needs to be conducted to understand the origin of the ferromagnetic moment.

We have been able to identify the transition from a antiferromagnetic hellical phase to a antiferromagnetic co-planar triangular phase in the xy-plane at T_t. This has been identified through a clear 6-fold oscillation in magnetization appearing above transition temperature T_t. Chiral anomaly of the triangular phase has been clearly confirmed through measurements of AHE, PHE and NMR. These exotic transport properties have all been found for $Mn_{3+\delta}Sn$, with varying Mn concentration before. However, never been all observed in one compound of Mn_3Sn. We have observed a clear difference in nature between the HE and PHE. Both effects have a clear jump at T_t, but have different charge carriers. Looking at the temperature dependence of all three effects, PHE, HE and MR, they seem to have a maximum right above the transition temperature, after which they begin to slowly diminish.

A weak ferromagnetism was also observed above T_t, with a field dependent easy direction, consistent with previous reports. We found that for low field, the easy magnetization direction for $Mn_{3.13}Sn$ is in the xy-plane at low field, moving to the z-direction ([0001]) at higher field. However, a part of this field dependence might be due to shape anisotropy. As a next step, we suggest to conduct a thorough field de-

pendence scan of the anisotropy, using a more symmetric crystal, and see if it would replicate the results found by T.F. Duan *et al.* [56], which were also conducted on a $Mn_{3.13}Sn$ sample. Magnetization curves, as well as Zero Field Heating results show that the nature of the weak ferromagnetism below T_f and above T_t differ in character, indicating that they do not arise from a similar magnetic structure.

To be able to utilize the exotic transport effects of Mn_3Sn, a systematic investigation of the transport properties and their dependence on composition, temperature and field need to be conducted. We have completed a first step in being able to map all the exotic transport phenomena found to the composition $Mn_{3.13}Sn$.

References

[1] M. König et al. “Quantum Spin Hall Insulator State in HgTe Quantum Wells”. In: *Science* 318.5851 (Nov. 2007), pp. 766–770. DOI: 10.1126/science.1148047.

[2] M. Z. Hasan and C. L. Kane. “Colloquium: Topological insulators”. In: *Rev. Mod. Phys.* 82 (4 Nov. 2010), pp. 3045–3067. DOI: 10.1103/RevModPhys.82.3045.

[3] B. A. Bernevig, C. Felser, and H. Beidenkopf. “Progress and prospects in magnetic topological materials”. In: *Nature* 7899 (Mar. 2022), pp. 41–51. DOI: 10.1038/s41586-021-04105-x.

[4] B. Yan and C. Felser. “Topological Materials: Weyl Semimetals”. In: *Annual Review of Condensed Matter Physics* 8 (Nov. 2016). DOI: 10.1146/annurev-conmatphys-031016-025458.

[5] V. Baltz et al. “Antiferromagnetic spintronics”. In: *Rev. Mod. Phys.* 90 (Feb. 2018). DOI: 10.1103/RevModPhys.90.015005.

[6] L. Smejkal et al. “Topological antiferromagnetic spintronics”. In: *Nature Physics* 14.3 (Mar. 2018), pp. 242–251. DOI: 10.1038/s41567-018-0064-5.

[7] M. Nakahara. *Geometry, Topology and Physics*. CRC Press, Oct. 2018. Chap. 2. DOI: 10.1201/9781315275826.

[8] H. Segerman. *Topological joke*. URL: https://www.shapeways.com/product/6CJQ9GXWW/topology-joke (visited on 05/29/2022).

[9] J.-P. Colinge and J. C. Greer. “Nanowire Electronic Structure”. In: *Nanowire Transistors*. Cambridge, England: Cambridge University Press, Apr. 2016. Chap. 5. DOI: 10.1017/CBO9781107280779.

[10] P. Kotetes. *Topological Insulators*. 2053-2571. Morgan & Claypool Publishers, 2019. ISBN: 978-1-68174-517-6. DOI: 10.1088/978-1-68174-517-6.

[11] M. V. Berry. “Quantal Phase Factors Accompanying Adiabatic Changes”. In: *Proceedings of the Royal Society A: Mathematical and Physical Sciences* 392.1802 (1984), pp. 45–57. DOI: 10.1098/rspa.1984.0023.

[12] J. K. Asbóth, L. Oroszlány, and A. Pályi. “Berry Phase, Chern Number”. In: *A Short Course on Topological Insulators*. Springer, 2016. Chap. 2, pp. 23–44. DOI: 10.1007/978-3-319-25607-8.

[13] D. N. Sheng et al. “Quantum Spin-Hall Effect and Topologically Invariant Chern Numbers”. In: *Phys. Rev. Lett.* 97 (3 July 2006), p. 036808. DOI: 10.1103/PhysRevLett.97.036808.

[14] H. Weyl. “Elektron und Gravitation. I”. In: *Z. Physik* 56 (May 1929), pp. 330–352. DOI: 10.1007/BF01339504.

[15] Y. Tang and A. E. Cohen. “Optical Chirality and Its Interaction with Matter”. In: *Phys. Rev. Lett.* 104 (16 Apr. 2010), p. 163901. DOI: 10.1103/PhysRevLett.104.163901.

[16] A. A. Burkov. “Giant planar Hall effect in topological metals”. In: *Phys. Rev. B* 96 (4 July 2017), p. 041110. DOI: 10.1103/PhysRevB.96.041110.

[17] B. A. Bernevig. “It’s been a Weyl coming”. In: *Nature Physics* 11.9 (Aug. 2015), pp. 698–699. DOI: 10.1038/nphys3454.

[18] O. Vafek and A. Vishwanath. “Dirac Fermions in Solids: From High-Tc Cuprates and Graphene to Topological Insulators and Weyl Semimetals”. In: *Annual Review of Condensed Matter Physics* 5 (Mar. 2014), pp. 83–112. DOI: 10.1146/annurev-conmatphys-031113-133841.

[19] T. Chen et al. “Anomalous transport due to Weyl fermions in the chiral antiferromagnets Mn_3X, X = Sn, Ge”. In: *Nature Communications* 12.1 (Jan. 2021). DOI: 10.1038/s41467-020-20838-1.

[20] N. H. Sung et al. “Magnetic phase dependence of the anomalous Hall effect in Mn_3Sn single crystals”. In: *Applied Physics Letters* 112.13 (Mar. 2018), p. 132406. DOI: 10.1063/1.5021133.

[21] S. Kurosawa et al. “Chiral-anomaly-driven magnetotransport in the correlated Weyl magnet Mn_3Sn”. In: (Apr. 2022). DOI: 10.48550/ARXIV.2204.00882.

[22] K. Kuroda et al. “Evidence for magnetic Weyl fermions in a correlated metal”. In: *Nature Materials* 16.11 (Sept. 2017), pp. 1090–1095. DOI: 10.1038/nmat4987.

[23] J. W. Cable, N. Wakabayashi, and P. Radhakrishna. “Structure of the modulated magnetic phase of Mn_3Sn”. In: *Journal of Applied Physics* 75 (May 1994), pp. 6601–6601. DOI: 10.1063/1.356908.

[24] L. M. Sandratskii and J. Kubler. “Role of Orbital Polarization in Weak Ferromagnetism”. In: *Phys. Rev. Lett.* 76 (26 June 1996), pp. 4963–4966. DOI: 10.1103/PhysRevLett.76.4963.

[25] E. Krén et al. “Study of the magnetic phase transformation in the Mn_3Sn phase”. In: *Physica B+C* 80.1 (1975), pp. 226–230. DOI: 10.1016/0378-4363(75)90066-2.

[26] N. J. Ghimire and I. I. Mazin. “Topology and correlations on the kagome lattice”. In: *Nature Materials* 19.2 (Jan. 2020), pp. 137–138. DOI: 10.1038/s41563-019-0589-8.

[27] W. J. Feng et al. “Glassy ferromagnetism Ni_3Sn-type $Mn_{3.1}Sn_{0.9}$”. In: *Phys. Rev. B* 73.20 (May 2006). DOI: 10.1103/PhysRevB.73.205105.

[28] J. J. Deng et al. “Effect of residual strain on magnetic properties and Hall effect in chiral antiferromagnet Mn3Sn”. In: *Journal of Physics D: Applied Physics* 55.27 (Apr. 2022), p. 275001. DOI: 10.1088/1361-6463/ac5da7.

[29] P. J. Brown et al. “Determination of the magnetic structure of Mn_3Sn using generalized neutron polarization analysis”. In: *Journal of Physics: Condensed Matter* 2.47 (Nov. 1990), pp. 9409–9422. DOI: 10.1088/0953-8984/2/47/015.

[30] K. H. Fischer and J. A. Hertz. “Preface”. In: *Spin Glasses*. Cambridge, England: Cambridge University Press, June 2011, pp. ix–x. DOI: 10.1017/CBO9780511628771.

[31] P. K. Rout et al. “Field-induced topological Hall effect in the noncoplanar triangular antiferromagnetic geometry of Mn_3Sn”. In: *Phys. Rev. B* 99 (9 Mar. 2019), p. 094430. DOI: 10.1103/PhysRevB.99.094430.

[32] A. Fert, N. Reyren, and V. Cros. “Magnetic skyrmions: advances in physics and potential applications”. In: *Nature Reviews Materials* 2.7 (June 2017). DOI: 10.1038/natrevmats.2017.31.

[33] J. Kübler and C. Felser. “Non-collinear antiferromagnets and the anomalous Hall effect”. In: *Europhysics Letters* 108.6 (Dec. 2014), p. 67001. DOI: 10.1209/0295-5075/108/67001.

[34] J. J. Quinn and K.-S. Yi. *Solid State Physics*. 2nd ed. Springer, 2018. DOI: 10.1007/978-3-319-73999-1.

[35] W. E. Liu, E. M. Hankiewicz, and D. Culcer. “Weak localization and antilocalization in topological materials with impurity spin-orbit interactions”. In: *Materials* 10.7 (July 2017), p. 807. DOI: 10.3390/ma10070807.

[36] V. F. Gantmakher. “Quantum Corrections to Conductivity”. In: *Electrons and Disorder in Solids*. Oxford University Press, Aug. 2005. Chap. 2, pp. 16–42. DOI: 10.1093/acprof:oso/9780198567561.001.0001.

[37] J. D. Patterson and B. C. Bailey. “Solid-State Physics”. In: 3rd ed. Basel, Switzerland: Springer, Jan. 2019. Chap. 6.1.5. DOI: 10.1007/978-3-319-75322-5.

[38] E. M. Pugh and N. Rostoker. “Hall Effect in Ferromagnetic Materials”. In: *Rev. Mod. Phys.* 25 (1 Jan. 1953), pp. 151–157. DOI: 10.1103/RevModPhys.25.151.

[39] N. Nagaosa et al. “Anomalous Hall effect”. In: *Rev. Mod. Phys.* 82 (2 May 2010), pp. 1539–1592. DOI: 10.1103/RevModPhys.82.1539.

[40] C. Goldberg and R. E. Davis. “New Galvanomagnetic Effect”. In: *Phys. Rev.* 94 (5 June 1954), pp. 1121–1125. DOI: 10.1103/PhysRev.94.1121.

[41] N. Kumar et al. “Planar Hall effect in the Weyl semimetal GdPtBi”. In: *Phys. Rev. B* 98 (4 July 2018), p. 041103. DOI: 10.1103/PhysRevB.98.041103.

[42] B. D. Cullity and C. D. Graham. “Magnetic Anisotropy”. In: *Introduction to Magnetic Materials*. Hoboken, NJ, USA: John Wiley & Sons, Inc., 2008. Chap. 7. DOI: 10.1002/9780470386323.

[43] C. Williams et al. “Torque measurements of the magnetic anisotropy energy of antiferromagnetic-coupled Fe/Cr/Fe layers”. In: *Journal of Magnetism and Magnetic Materials* 110.1 (1992), pp. 61–64. ISSN: 0304-8853. DOI: 10.1016/0304-8853(92)90012-D.

[44] D. Martien. *AC Susceptibility*. visited on 2022-05-15. URL: https://qdusa.com/siteDocs/appNotes/1078-201.pdf.

[45] *Magnetic Measurement Techniques for Materials Characterization*. 1st ed. Cham, Switzerland: Springer, Sept. 2021. Chap. 1.

[46] H. Weinstock, ed. *SQUID sensors*. 1st ed. Berlin, Germany: Springer, 1996. DOI: 10.1007/978-94-011-5674-5.

[47] *SQUID Magnetometer*. visited on 2022-04-25. URL: https://www.qdusa.com/products/mpms3.html.

[48] J. Clarke and A. I. Braginski, eds. *The SQUID handbook*. Weinheim, Germany: Wiley-VCH Verlag, May 2004. DOI: 10.1002/3527603646.

[49] M. Sawicki, W. Stefanowicz, and A. Ney. “Sensitive SQUID magnetometry for studying nanomagnetism”. In: *Semiconductor Science and Technology* 26.6 (Apr. 2011), p. 064006. DOI: 10.1088/0268-1242/26/6/064006.

[50] C. Dennis, R. Shull, and N. Matsumoto. “Improvement of Reproducibility of Magnetic Moment Detected by a SQUID Magnetometer Through Radial Offset Measurement on a YIG Sphere”. In: *IEEE Transactions on Magnetics* 55.2 (Feb. 2019). DOI: 10.1109/TMAG.2018.2867477.

[51] *MPMS,PPMS*. visited on 2022-05-06. URL: https://www.fz-juelich.de/jcns/jcns-2/EN/Leistungen/PPMS-MPMS/_node.html.

[52] *Physical Property Measurement System Quantum Design PPMS DynaCool*. visited on 2022-05-06. URL: https://www.qdusa.com/products/dynacool.html.

[53] *Horizontal Rotator*. visited on 2022-05-10. URL: https://www.qdusa.com/siteDocs/productBrochures/1084-500_PPMS_Horizontal%20Rotator.pdf.

[54] *MPMS3 Options*. visited on 2022-05-02. URL: https://www.qdusa.com/siteDocs/productBrochures/1505-603.pdf.

[55] *Laue Camera*. visited on 2022-05-31. URL: https://www.fz-juelich.de/en/jcns/jcns-2/expertise/in-house-x-ray/laue-camera.

[56] T. F. Duan et al. “Magnetic anisotropy of single-crystalline Mn_3Sn in triangular and helix-phase states”. In: *Applied Physics Letters* 107.8 (Aug. 2015). DOI: 10.1063/1.4929447.

[57] R. Reed and A. F. Clark. “Materials at Low Temperatures”. In: *Temperature Dependence of Resistivity (Metals)*. ASM International, 1983. Chap. 14.3.2.2. ISBN: 0871701464.

[58] I. A. Cohn et al. “Magnetoresistance in Quasi-One-Dimensional Weyl Semimetal $(TaSe_4)_2I$”. In: *JETP Letters* 112.2 (July 2020). DOI: 10.1134/s0021364020140040.